

Evaluating the phase dynamics of coupled oscillators via time-variant topological features

Kazuha Itabashi,^{*} Quoc Hoan Tran,[†] and Yoshihiko Hasegawa[‡]

*Graduate School of Information Science and Technology,
The University of Tokyo, Tokyo 113-8656, Japan*

(Dated: December 1, 2021)

The characterization of phase dynamics in coupled oscillators offers insights into fundamental phenomena in complex systems. To describe the collective dynamics in the oscillatory system, order parameters are often used but are insufficient for identifying more specific behaviors. We therefore propose a topological approach that constructs quantitative features describing the phase evolution of oscillators. Here, the phase data are mapped into a high-dimensional space at each time point, and topological features describing the shape of the data are subsequently extracted from the mapped points. We extend these features to time-variant topological features by considering the evolution time, which serves as an additional dimension in the topological-feature space. The resulting time-variant features provide crucial insights into the time evolution of phase dynamics. We combine these features with the machine learning kernel method to characterize the multicluster synchronized dynamics at a very early stage of the evolution. Furthermore, we demonstrate the usefulness of our method for qualitatively explaining chimera states, which are states of stably coexisting coherent and incoherent groups in systems of identical phase oscillators. The experimental results show that our method is generally better than those using order parameters, especially if only data on the early-stage dynamics are available.

I. INTRODUCTION

Coupled phase oscillators have been widely used to investigate cooperative behaviors in complex systems. The coupling scheme of the oscillators in nature are reflected by the dynamic behaviors of complex systems, which include chimera state emergence, chaos, multistability, and synchronization. For example, a brain network can be analyzed as a coupling model of ten billion neurons, which can exhibit chimera-like states with responses relating to certain brain disorders [1–3]. Meanwhile, circadian clock systems, in which a synchronized state and an asynchronized state interchange within a one-day cycle, are related to other diseases such as metabolic disorders, cataplexy, and narcolepsy [4, 5]. Electromechanical systems can also behave as chaotic oscillators, and gaining an appropriate understanding of oscillator dynamics thus promotes the realization of these systems, which can operate in a noisy environment [6, 7]. One of the primary points of interest related to coupled oscillators is the prediction of the attendant dynamics from data obtained at the early stage of the system. Because many collective dynamics can be modeled by coupled oscillators, the early prediction of coupled oscillator dynamics has good potential for applications such as the diagnosis of human diseases and the detection of specific malfunctions. However, the realization of these applications requires the adoption of theoretical and computational methods to adequately represent the time profile of coupled oscillators.

The intrinsic dynamic properties of coupled oscillators are often described in terms of their phase variables. Meanwhile, the degree of the global synchronization of the system is commonly expressed by the Kuramoto order parameter, which represents the phase coherence of the oscillators. The Kuramoto order parameter takes the value of 0 for complete asynchronization and up to 1 for full synchronization [8]. However, the order parameter method is insufficient for effectively analyzing the synchronization situation under certain conditions. For example, when the value of the order parameter is 0, the oscillators can be synchronized in terms of a symmetrical phase distribution even though they should, by definition, be completely asynchronous. In view of this, rather than use specific global parameters to represent the collective dynamics, our approach focuses on the topological aspects of specific phase variables to reveal the phase dynamics along the evolution timeline in terms of more efficient quantities. First, at each oscillator, we define a phase-dependent point in a high-dimensional space. We then focus on the time-variant evolutionary change in the shape of these points known as a *point cloud* $\mathcal{P}(t)$ within the space. We hypothesized that this evolutionary change has a close relationship with pattern formation, signal propagation, and the stochastic phenomena and extensive chaos in oscillatory systems. Thus, we demonstrate that tracking these changes can provide crucial insights into the dynamics at the early stage of the system.

The basic idea of our approach is that topological aspects can help to reveal the underlying structure of the collective patterns of oscillators as the system evolves. Here, we apply persistent homology analysis [9] to evaluate the configuration of $\mathcal{P}(t)$ in terms of quantitative topological features and to monitor the variation of these features throughout time t for application in the task of

^{*} itabashi@biom.t.u-tokyo.ac.jp

[†] k09tranhoan@gmail.com

[‡] hasegawa@biom.t.u-tokyo.ac.jp

predicting the dynamics. Persistent homology is a technique from algebraic topology in approaches aimed at representing the shape of the data related to the information on the topological structures, such as the connected components, loops, or holes in the data. Persistent homology has been effectively applied to studying the qualitative changes in data from various dynamical systems, including time series [10, 11], time-varying networks [12–14], and quantum data [15]. Given a non-negative threshold ε , we place ε -radius balls centered at points in $\mathcal{P}(t)$ and observe the shape of the space overlapped by these balls [Fig. 1(a)]. At a sufficiently small ε , we can obtain the shape without any difference between the original points in the point cloud. When we increase ε , the balls intersect, which subsequently leads to the change in the topological structures in terms of, for example, the connected components or loops in the space. Here, the connected components tend to merge, while loops emerge and then vanish in accordance with the gradual change in the threshold. At each time point, we define the topological features as the values of ε to represent the emergence and disappearance of the topological structures [Fig. 1(b)]. Furthermore, we extend these features by adding the time axis [Fig. 1(c)].

These extended features, referred to as time-variant topological features, can reflect the temporal behavior of the oscillators and can therefore provide useful knowledge for predicting the dynamics at the early stage of the system. In fact, these features can serve as discriminate features in qualitative evaluations of the phase dynamics of oscillators. We can input these features into the machine learning kernel algorithms to allow for the application of statistical-learning tasks, which include classifying the behaviors of multicluster synchronization or predicting chimera states in which synchronization and asynchronization co-exist. Interestingly, our approach characterizes the phase dynamics of oscillators at a very early stage of the time evolution, a point where conventional order parameters do not effectively operate.

II. METHODS

A. Time-variant topological features

To explain the proposed time-variant topological features, we considered the Kuramoto model, which is the most common and best-suited model for understanding synchronization phenomena in physical, chemical, and biological systems. Given a set of N coupled heterogeneous oscillators, the Kuramoto model was formalized as a set of first-order differential equations:

$$\frac{d\theta_i}{dt} = \omega_i + \frac{1}{N} \sum_{j=1}^N g_{ij} \sin(\theta_j - \theta_i - \alpha). \quad (1)$$

Here, θ_i and ω_i denote the phase and the natural frequency of the oscillator i , respectively, and $g_{ij} \geq 0$ rep-

resents the coupling strength between oscillators i and j . The angle α is a tunable parameter describing the phase lag between oscillators i and j .

To study the dynamics of the coupled oscillators, we considered a mapping φ from the set $\{\theta_1(t), \theta_2(t), \dots, \theta_N(t)\}$ of phases to the set $\mathcal{P}_\varphi(t) = \{\mathbf{s}_1(t), \mathbf{s}_2(t), \dots, \mathbf{s}_N(t)\}$ of points in a specific L -dimensional space \mathbb{R}^L , where $\mathbf{s}_i(t) = \varphi(\theta_i(t)) \in \mathbb{R}^L$. By considering an appropriate mapping φ , the information on the evolutionary change in the configuration of $\mathcal{P}_\varphi(t)$ along t can provide important insights into the dynamics of coupled oscillators. Our approach to quantifying the configuration of $\mathcal{P}_\varphi(t)$ into quantitative features relies on the persistent homology theory. First, we defined a distance function $d_\varphi : \mathcal{P}_\varphi(t) \times \mathcal{P}_\varphi(t) \rightarrow \mathbb{R}$ to evaluate the dissimilarity between oscillators i and j at time t . We centered a ε -radius ball at each point $\mathbf{s}_i(t)$ in $\mathcal{P}_\varphi(t)$, i.e., to form the set $B(\varepsilon, \mathbf{s}_i(t)) = \{\mathbf{v} \in \mathbb{R}^L \mid d_\varphi(\mathbf{s}_i(t), \mathbf{v}) \leq \varepsilon\}$. Then, by taking the union of these balls over all $i = 1, 2, \dots, N$, we could obtain an overlapped space,

$$\mathcal{U}(\varepsilon, \mathcal{P}(t)) = \bigcup_{i=1}^N B(\varepsilon, \mathbf{s}_i(t)), \quad (2)$$

the shape of which represents the configuration of $\mathcal{P}_\varphi(t)$ at the radius ε . The idea of persistent homology is to track how this shape changes as the radius ε increases.

In fact, the method allows for modeling the shape of $\mathcal{U}(\varepsilon, \mathcal{P}_\varphi(t))$ in a far more mathematically and computationally tractable representation, i.e., a simplicial complex, which is a complex of geometric structures known as simplices. Here, an n -simplex presents a generalization of the notion of a triangle or tetrahedron to arbitrary dimensions. For example, a 0-simplex is a point, a 1-simplex is a line segment (with two end points as its faces), and a 2-simplex is a triangle and its enclosed area (with three edges and three vertices as its faces). Similarly, a 3-simplex is a filled tetrahedron (with triangles, edges, and vertices as its faces), and while a 4-simplex is beyond visualization, it is a filled shape with tetrahedrons, triangles, edges, and vertices as its faces. One of the main types of simplicial complexes is known as the Vietoris–Rips complex, which we will now briefly review. A Vietoris–Rips complex $V_R(\varepsilon, \mathcal{P}_\varphi(t))$ is a collection of simplices, where each simplex is built over a subset of points in $\mathcal{P}_\varphi(t)$ if $B(\varepsilon, \mathbf{s}_i(t)) \cap B(\varepsilon, \mathbf{s}_j(t)) \neq \emptyset$ for every pair of points $\mathbf{s}_i(t), \mathbf{s}_j(t)$ in the subset. Now, starting with $\varepsilon = 0$, the complex contains only the 0-simplices, i.e., the discrete points. As ε increases, connections emerge between the points and the edges (1-simplices), and filled triangles (2-simplices) are introduced into the complexes [Fig. 1(a)]. This process enables us to obtain a sequence of embedded complexes, which is defined as a filtration. Moreover, if ε becomes considerably large, all the points become interconnected, which means no useful information can be conveyed.

As noted above, persistent homology is focused on the emergence and disappearance of topological structures

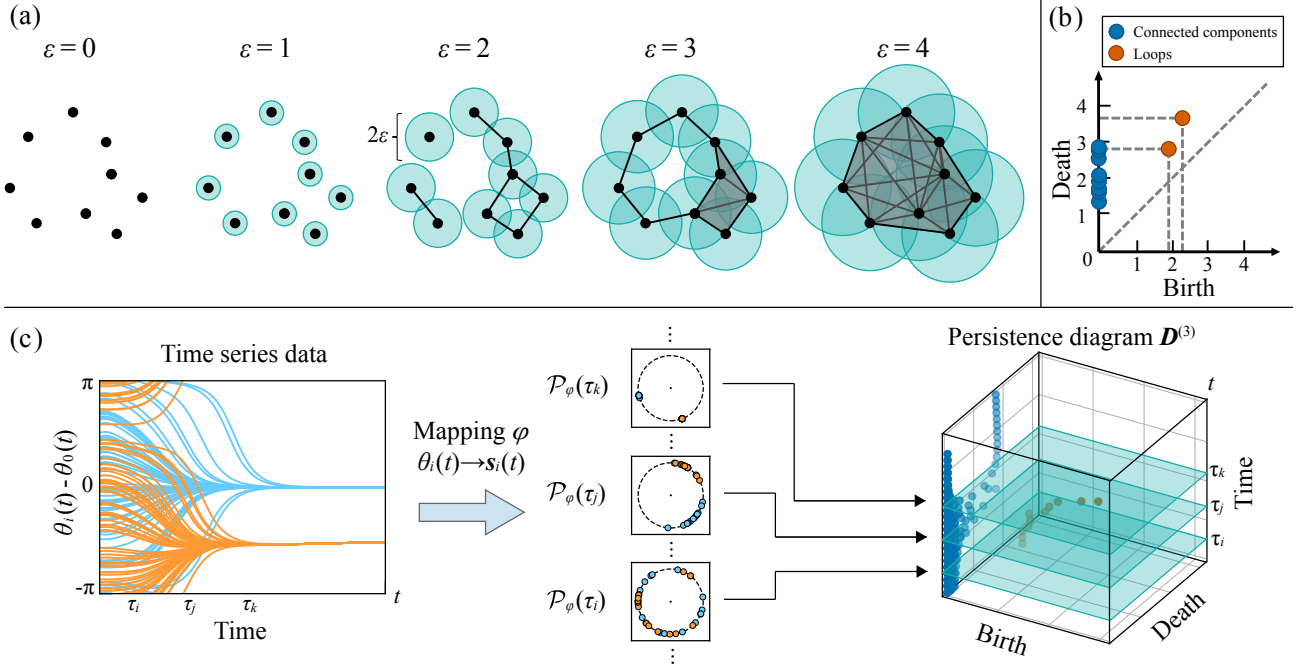


FIG. 1. Illustration of time-variant topological features for coupled oscillator systems. (a) Example of a sequence of the Vietoris–Rips complex, i.e., a filtration constructed from a set of discrete points. Each ball of radius ϵ was placed at each point, then, the Vietoris–Rips complex was used to model the shape of the union of these balls. In the complex, each simplex is formed from a subset of points if every pair of corresponding balls intersect. The evolution changes in the topological structures, e.g., the merging of connected components and the emergence and disappearance of loops, were tracked through increasing the ϵ until no change was observed. At $\epsilon = 0$, there were nine points corresponding with nine connected components in the space. At $\epsilon = 2$, several edges were added into the complex, at which point a number of connected components perished and merged. Similarly, two loops emerged in the space at birth radii $\epsilon = 2$ and $\epsilon = 3$, respectively, and then perished at death radii $\epsilon = 3$ and $\epsilon = 4$, respectively. (b) The collection of birth and death radii is represented in a two-dimensional *persistence diagram*. (c) At each time step, the coupled oscillator phases were mapped into a set of discrete points, i.e., a point cloud within a metric space. The two-dimensional persistence diagram was constructed from this point cloud for each time step. Time-variant topological features were obtained by concatenating these diagrams across the time steps into a three-dimensional persistence diagram.

such as any connected components and loops in the filtration. For example, in Fig. 1(a), while there are nine connected components in the space at $\epsilon = 0$ and $\epsilon = 1$, at $\epsilon = 2$, several components are merged together, meaning three connected components remain in the space. Similarly, one loop exists in the space from $\epsilon = 2$ to $\epsilon = 3$, and one in the space from $\epsilon = 3$ to $\epsilon = 4$. These topological structures are mathematically represented by the concept of the dimension 0 and dimension 1 persistent homology groups, which are vector spaces with dimensions corresponding to the number of connected components and the number of loops, respectively (see [16] for more details). We use the emergence and disappearance of these topological structures in the filtration to quantify the evolution in the shape of $\mathcal{U}(\epsilon, \mathcal{P}_\varphi(t))$. Here, each of the connected components and loops was assigned to a persistence pair of radius (ϵ_b, ϵ_d) , such that they originated at the birth radius $\epsilon = \epsilon_b$ and perished at the death radius $\epsilon = \epsilon_d$. The collection of all persistence pairs in a two-dimensional coordinate system presents a two-dimensional persistence diagram $D^{(2)}(\mathcal{P}_\varphi(t))$, which contains topological features for $\mathcal{P}_\varphi(t)$ [Fig. 1(b)]. To map

the dynamic properties of coupled oscillators into topological features, we proposed using time-variant topological features containing time-related information on the dynamics in addition to the birth radius and death radius. We extended two-dimensional persistence diagrams into three-dimensional persistence diagrams as

$$D^{(3)}(\varphi) = \{(\epsilon_b, \epsilon_d, \tau) \mid (\epsilon_b, \epsilon_d) \in D^{(2)}(\mathcal{P}_\varphi(\tau)), \tau = \tau_1, \tau_2, \dots, \tau_T\}. \quad (3)$$

Here, a three-dimensional persistent diagram is formed by concatenating two-dimensional diagrams along the time-axis at time steps $\tau_1 < \tau_2 < \dots < \tau_T$ [Fig. 1(c)].

B. Kernel method for topological features

In machine learning tasks using time-variant topological features, we are typically provided with a collection of inputs $\mathcal{D} = \{D_1, \dots, D_M\}$ from a certain set of diagrams, from which we must quantify any patterns to evaluate previously unseen data. Since a persistence diagram is a multiset of points of variable size, it can be

difficult to apply the algorithms when considering the inputs as vectors or when requiring the inner product form of calculation for the input data. Here, we employed kernel methods that use a similarity measure $\kappa(\mathbf{D}_i, \mathbf{D}_j)$ between any two diagrams $\mathbf{D}_i, \mathbf{D}_j \in \mathcal{D}$. More precisely, a function $\kappa : \mathcal{D} \times \mathcal{D} \rightarrow \mathbb{R}$ is called a kernel if the Gram matrix K with entries $K_{ij} = \kappa(\mathbf{D}_i, \mathbf{D}_j)$ is positive semidefinite. To define the kernel, a feature map Φ was considered in view of mapping a diagram $\mathbf{D}_i \in \mathcal{D}$ to a vector $\Phi(\mathbf{D}_i)$ in a Hilbert space \mathcal{H}_b wherein we could define the inner product $\langle \cdot, \cdot \rangle_{\mathcal{H}_b}$ on \mathcal{H}_b . Every feature map Φ defines the kernel $\kappa(\mathbf{D}_i, \mathbf{D}_j) := \langle \Phi(\mathbf{D}_i), \Phi(\mathbf{D}_j) \rangle_{\mathcal{H}_b}$. Several proposals have been forwarded to define a kernel for two-dimensional diagrams, including the persistence scale space kernel [17], which is based on the heat diffusion kernel, the persistence weighted Gaussian kernel [18], which emerged from kernel mean embedding, the sliced Wasserstein kernel under Wasserstein geometry [19], and the persistence Fisher kernel [20], which relies on Fisher information geometry. Here, we extended the persistence Fisher kernel to define a kernel for three-dimensional persistence diagrams, which we briefly review below.

The persistence Fisher kernel considers each persistence diagram as the sum of normal distributions and then measures the similarity between the distributions via the Fisher information metric. Let $\mathbf{D}_{i\Delta}$ and $\mathbf{D}_{j\Delta}$ be the point sets obtained by projecting two persistence diagrams \mathbf{D}_i and \mathbf{D}_j on the diagonal line $y = x$ of the Cartesian plane. The kernel compares two extended persistence diagrams, $\mathbf{D}'_i = \mathbf{D}_i \cup \mathbf{D}_{j\Delta}$ and $\mathbf{D}'_j = \mathbf{D}_j \cup \mathbf{D}_{i\Delta}$, which have the same number of points. The summation of normal distributions on \mathbf{D}'_i can be defined as $\rho_{\mathbf{D}'_i} = \sum_{\mathbf{u} \in \mathbf{D}'_i} \frac{1}{Z} \mathcal{N}(\mathbf{u}, \nu \mathbf{I})$. Here, \mathcal{N} is a Gaussian function with bandwidth ν , \mathbf{I} is an identity matrix, and $Z = \int_{\Omega} \sum_{\mathbf{u} \in \mathbf{D}'_i} \mathcal{N}(\mathbf{x}; \mathbf{u}, \nu \mathbf{I}) d\mathbf{x}$ is the normalization constant with the integral calculated on $\Omega = \mathbf{D}_i \cup \mathbf{D}_{i\Delta} \cup \mathbf{D}_j \cup \mathbf{D}_{j\Delta}$. Given a positive scalar α , the persistence Fisher kernel is defined as

$$\kappa_F(\mathbf{D}_i, \mathbf{D}_j) = \exp(-\alpha d_F(\mathbf{D}_i, \mathbf{D}_j)), \quad (4)$$

where $d_F(\mathbf{D}_i, \mathbf{D}_j) = \arccos \left(\int_{\Omega} \sqrt{\rho_{\mathbf{D}'_i}(\mathbf{x}) \rho_{\mathbf{D}'_j}(\mathbf{x})} d\mathbf{x} \right)$ is the Fisher information metric between $\rho_{\mathbf{D}'_i}$ and $\rho_{\mathbf{D}'_j}$.

III. RESULTS

A. Multicluster synchronization

A network system of multiple coupled oscillators can demonstrate multicluster synchronization, i.e., the network may split into several clusters of independent synchronized or organized behavior rather than form an entire system of synchronized behavior. Multicluster synchronizations are found in asymptotic states [21–23], in transient states [24], and in modular and hierarchical

structures [25]. Here, we demonstrate that our time-variant topological features obtained at the early stage of the dynamics can help to predict the multicluster synchronized behavior of oscillators.

We consider three oscillator networks with different configurations of coupling strength g_{ij} as presented in Eq. (1): the globally coupled network where all coupling strengths are equal [Fig. 2(a)], the modular coupled networks with two [Fig. 2(b)] and four modules [Fig. 2(c)]. We set the coupling strength $g_{ij} = 2$ for $\forall i \neq j$ for the globally coupled network. In the modular coupled networks, the coupling strengths of the oscillators belonging to the same module were different from those belonging to the different modules. We set $g_{ij} = 2$ for the oscillators in the same module, and $g_{ij} = 0.01$ for those belonging to the different modules. Here, we set the number of oscillators as $N = 128$, the angular frequency of i th oscillator as $\omega_i = 1$, and the tunable parameter as $\alpha = 0$. Corresponding with these configurations, different behaviors of synchronization, including single-cluster [Fig. 2(d)], two-cluster [Fig. 2(e)], and four-cluster synchronization [Fig. 2(f)], appear as $t \rightarrow \infty$.

We numerically solved Eq. (1) with randomly initialized phases $\theta_j(0) \in [0, 2\pi)$ and recorded the phases $\theta_j(t)$ at each time interval $\Delta\tau = 0.8$. We then used time sequences of $\mathcal{T}_T = \{\tau_1, \tau_2, \dots, \tau_T\}$ for the persistence diagram calculations, where $\tau_1 = 0, \tau_{k+1} - \tau_k = \Delta\tau$ ($k = 1, 2, \dots, T-1$), and T is the number of time steps. To calculate the time-variant topological features, we considered the mapping $\varphi : \theta \rightarrow (\cos \theta, \sin \theta)$ to transform the set of oscillator phases $\{\theta_1(t), \theta_2(t), \dots, \theta_N(t)\}$ to the point cloud $\mathcal{P}_{\varphi}(t) = \{\mathbf{s}_1(t), \mathbf{s}_2(t), \dots, \mathbf{s}_N(t)\}$, where $\mathbf{s}_j(t) = (\cos \theta_j(t), \sin \theta_j(t))$ lay on the unit circle in two-dimensional space. We adopted the distance function between $\mathbf{s}_j(t)$ and $\mathbf{s}_k(t)$ as the shortest distance between them measured along the unit circle.

Figure 3 shows examples of the time-variant topological features obtained from the globally [Fig. 3(a)], two-module [Fig. 3(b)], and four-module coupled [Fig. 3(c)] networks. Here, the temporal transition in the dynamics can be observed in terms of the transition in the temporal patterns of the topological features. On the top row of Fig. 3, the orange points represent the loops formed along the phase evolution timeline. For the globally coupled network, the loops quickly disappeared as the oscillators approached a synchronized state. In contrast, for the modular coupled networks, the birth radii of the loops increased as the oscillators were divided into multisynchronized clusters, which were uniformly dispersed. We considered the evolution of the topological features in terms of the connected components. The birth radius of each connected component was zero since N components corresponding to N oscillators appeared first. Therefore, we focused on the evolution of the death radii as illustrated in the bottom row of Fig. 3. Here, the colored bar in each plot represents the density in the distribution of the death radius. As represented by the right column inside each plot, at a sufficiently large time step, one

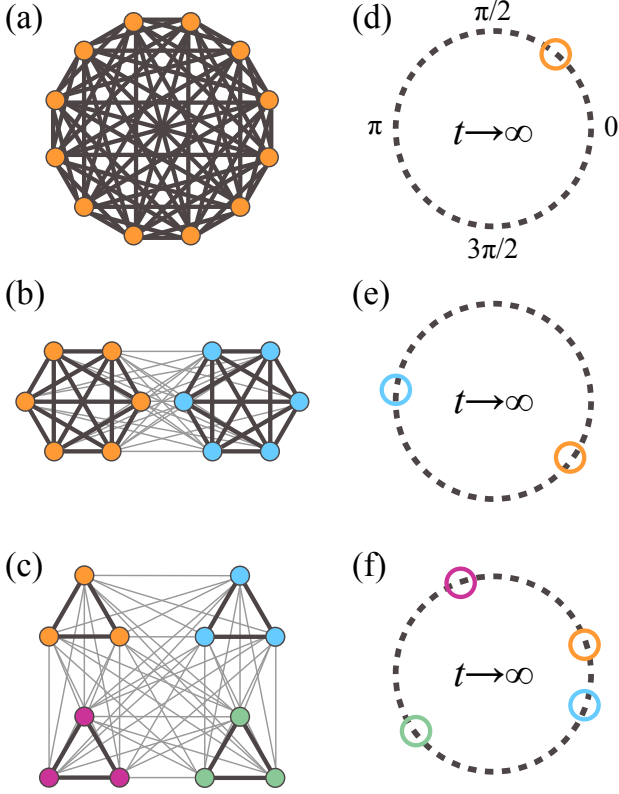


FIG. 2. The schematic of oscillator networks with different coupling configurations and the corresponding synchronization behaviors at infinite time. The vertices and edges in (a), (b), and (c) represent the oscillators and their coupling relations. The edges with bold lines imply strong coupling ($g_{ij} = 2$), while those with thin lines imply weak coupling ($g_{ij} = 0.01$). (a) All of the oscillators were symmetrically interactive and were globally coupled with the same coupling strength. The network had (b) two or (c) four modules, where the coupling strength of the oscillators in the same module was stronger than those belonging to the different modules. The oscillators exhibited different synchronized behaviors, including (d) single-cluster, (e) two-cluster, and (f) four-cluster synchronization, as $t \rightarrow \infty$.

connected component always retained the infinite value of the death radius. To distinguish the synchronized behavior of each coupling configuration, we examined the merging process of other connected components along the evolution timeline. In terms of the globally coupled network, the connected components quickly merged to form one component since the oscillators approached forming one synchronized-state cluster. At $t > 8$, only one component existed [Fig. 3(a)]. If the oscillators were distributed in terms of multiclusters in the synchronized state, more connected components existed for a longer period of time. The number of such components corresponded with the number of clusters in the synchronized state. For example, two connected components survived for a period of time of $t = 20$ to $t = 50$ [Fig. 3(b)], while four connected components survived for a period

of $t = 30$ to $t = 50$ [Fig. 3(c)]. These values corresponded with the behaviors of two-cluster [Fig. 3(b)] and four-cluster [Fig. 3(c)] synchronization, respectively.

Next, we applied the kernel method to characterize the differences among the synchronized behaviors of oscillators. It should be noted that our approach does not require prior labeling for the synchronization behaviors; rather, the focus is on characterizing the differences in the kernel space. This approach aligns with the unsupervised learning schemes, which are fundamentally different to the supervised learning schemes often used in machine learning methods. In the supervised learning schemes, the learning machine is trained on samples with predefined labels before the machine then attempts to predict an unknown label of a given sample, demonstrating that it has learned by generalizing to samples it has not encountered before. In contrast, unsupervised schemes do not require prior labelling but characterize the unknown dynamics via dimensional reduction methods. Here, we employed the persistence Fisher kernel described in Eq. (4) for the three-dimensional persistence diagrams. The synchronized behaviors were identified via the dimensional reduction method of kernel principal component analysis [26].

In our experiments, for each of the coupling configurations, we prepared 100 random initializations for the oscillator phases. Here, different types of synchronization, including single-cluster, two-cluster, and four-cluster synchronization, appear as $t \rightarrow \infty$. We used a time sequence of $\mathcal{T}_T = \{\tau_1, \tau_2, \dots, \tau_T\}$ for the persistence diagram calculations, where $\tau_1 = 0$, $\tau_{k+1} - \tau_k = 0.8$ ($k = 1, 2, \dots, T-1$). The number T controls the period of time to be used to detect the synchronized behaviors. We computed the Gram matrix for a total of 300 three-dimensional persistence diagrams. Figure 4(a) highlights the projection up to the third component of the kernel principal component analysis for the Gram matrix. Here, the purple, blue, and orange points represent the configurations with single-cluster, two-cluster, and four-cluster synchronization, respectively. At the very early stage, where, for example, $T = 4$, it was difficult to observe the clear difference between the points belonging to different groups of synchronized behaviors. However, the separability increased as we increased T to $T = 7, 9, 11$.

Accordingly, we could quantify the extent to which the time-variant topological features identify the synchronization behaviors better than the order parameters. Here, we constructed the following temporal sequence of Kuramoto order parameters: $\{r(\tau_1), r(\tau_2), \dots, r(\tau_T)\}$, where the Kuramoto order parameter is defined as $r(t) = \frac{1}{N} \left| \sum_{j=1}^N e^{i\theta_j(t)} \right|$. The Kuramoto order parameter takes the value of $[0, 1]$ and $r(t) = 1$ if the oscillators are in complete synchronization. We used the supervised learning scheme to compare the performance between the method using time-variant topological features and that using temporal Kuramoto order parameters. For each type of coupling configuration, we randomly split 100

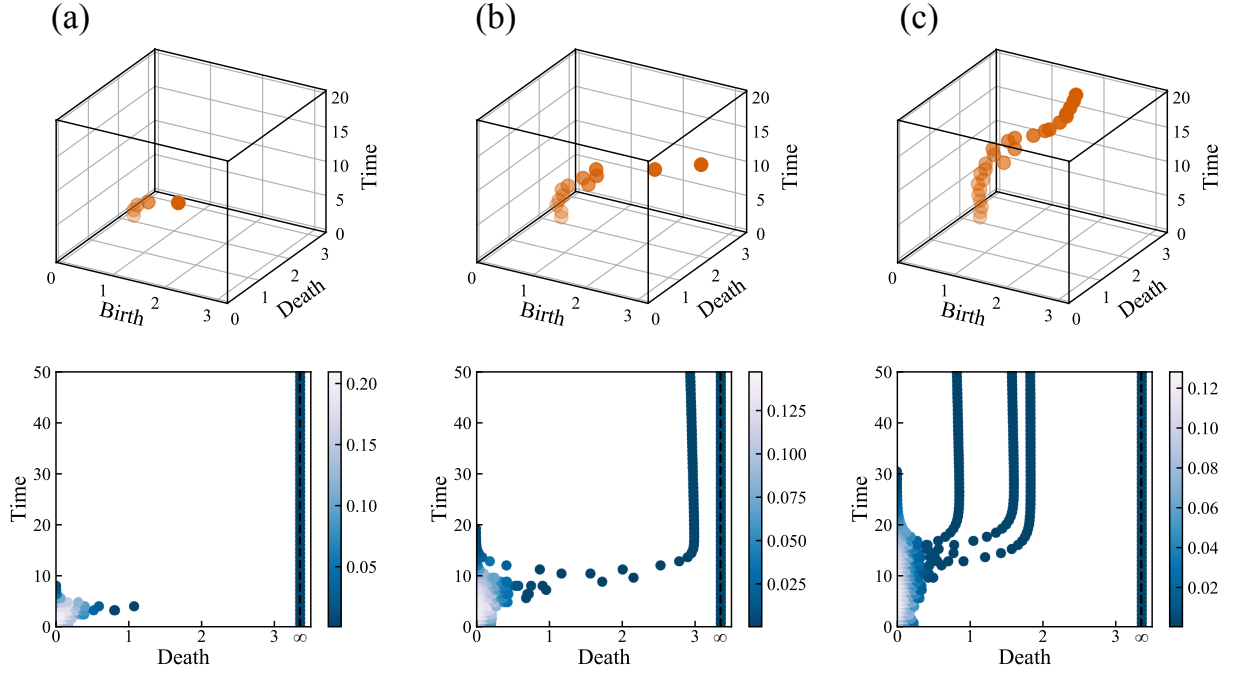


FIG. 3. Examples of time-variant topological features corresponding to the coupling oscillator dynamics in Fig. 2 (a), (b), and (c), respectively. The top row illustrates the three-dimensional persistence diagrams for the loop patterns, while the bottom row illustrates the distribution of the death radii of the connected components appearing along the phase evolution of the oscillators. As the oscillators approached forming one synchronized-state cluster, the loops quickly disappeared, and the connected components quickly merged to form one component [Fig. 3(a)]. As the oscillators tended to be divided into multicusters of synchronized state, the birth radii of the loops increased, and more connected components survived for a longer period of evolution time [Fig. 3(b)(c)]. The number of connected components surviving for a longer period of time corresponded with the number of clusters that were in the synchronized state.

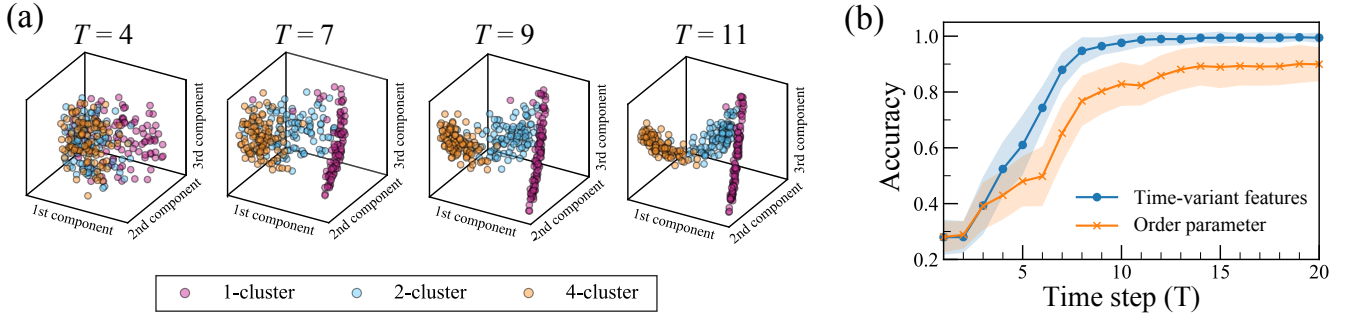


FIG. 4. (a) The kernel principal component projection of time-variant topological features obtained from $\tau = \tau_1, \tau_2, \dots, \tau_T$, where $\tau_1 = 0, \tau_{k+1} - \tau_k = \Delta\tau = 0.8$ ($k = 1, 2, \dots, T-1$). Here, T is the number of time steps. We illustrate the projection with $T = 4, 7, 9, 11$ from left to right. The different colors represent the realization of data with different synchronization schemes as single-cluster (purple), two-cluster (blue), and four-cluster (orange) synchronization. (b) The classification of synchronized states using time-variant topological features (blue line) or temporal Kuramoto order parameters (orange line). The lines depict the average test accuracy across 100 random train-test splits at each value of T . For each split, we randomly split 100 realizations into 75 realizations for training and 25 realizations for testing. The shaded areas indicate the confidence intervals of one standard deviation calculated using the same ensemble of runs.

realizations into 75 realizations for training and 25 realizations for testing. We then applied the support vector machine [27] for the classification where the input data were the kernel Gram matrices of the persistence diagrams or the vectors of the Kuramoto order parameters. Here, we classified the data into three labels that corre-

sponded with single-cluster, two-cluster, and four-cluster synchronization, then recorded the accuracy in identifying the true labels of the test data.

Figure 4(b) depicts the average test accuracy over 100 train-test random splits at each value of T . Here, we plotted the topological method using time-variant topo-

logical features (blue line), and the order method using order parameters (orange line). The shaded area indicates the confidence intervals of one standard deviation calculated using the same ensemble of runs. In general, increasing T served to increase the accuracy level for both methods since more information on the phase evolution was gathered. As Fig. 4(b) shows, the topological method demonstrated reasonably high accuracy in identifying the synchronized states, even in the early stage of the dynamics, i.e., over 85% when $T \geq 7$. It is clear that the corresponding accuracy of the order method was, at most, 65% at $T = 7$. As T was increased, the oscillator phases converged into synchronized states, and with a sufficiently large T ($T \geq 10$), the topological method achieved an approximate 100% accuracy, while the order method yielded an accuracy of, at best, 90%. These results validate the effectiveness and the reliability of time-variant topological features in capturing the differences among the future dynamics of oscillatory systems.

B. Chimera states

We applied the time-variant topological features to investigate the evolution of both the coherent and the incoherent dynamics in oscillatory systems, including the chimera states. A chimera state refers to a state where oscillators emerge to form two regions of mutually coherent and incoherent populations [28, 29]. Chimera states were initially explored in terms of homogeneous oscillator systems [30, 31], before they were then demonstrated experimentally [32, 33] to establish their connection with real-world systems such as the human brain networks [34]. With reference to Refs. [35, 36], we generated chimera states for the Kuramoto model by setting the coupling strength g_{ij} described in Eq. (1) as follows:

$$g_{ij} = \begin{cases} \frac{\pi}{2\gamma}, & \text{if } \cos\left(\frac{2\pi(i-j)}{N}\right) > \cos(\pi\eta) \\ 0, & \text{otherwise} \end{cases}. \quad (5)$$

Here, γ is a tunable parameter characterizing the coupling strength among the oscillators, and $\eta \in [0, 1]$ is a parameter used to control the range of the non-local coupling. In our numerical simulation, we set $N = 256$, $\omega_i = 0$, $\alpha = 1.39$, $\eta = 0.6$, and $\gamma = 0.6$ (for synchronized and chimera states) and $\gamma = 6$ (for asynchronized states).

The coherence-incoherence transition is illustrated by the time trace of the local order parameter [37, 38] defined at each oscillator as follows:

$$l_j(t) = \left| \frac{1}{2\delta + 1} \sum_{|j-k| \leq \delta} e^{i\theta_k(t)} \right|, \quad (6)$$

where $j = 1, 2, \dots, N$, and θ_k represents the phase of oscillator k in a region of side length $2\delta + 1$ centered at oscillator j . The local order parameter quantifies the degree of the coherent and incoherent regions around each

oscillator and yielded the local properties of the chimera states. More specifically, oscillator j at time t belongs to the coherent domain where $l_j(t) \approx 1$, or the incoherent domain where $l_j(t)$ has much lower values. Figure 5(a) shows three time profile examples for the local order parameters with $\delta = 12$. In the first example, $l_j(t)$ were close to 1 for all j and $t > 10$, which means it can be concluded that the oscillators entered global synchronization as $t > 10$. In the second example, the values of $l_j(t)$ for $80 \leq j \leq 200$ were lower than 0.6, while the other $l_j(t)$ were higher than 0.8 when $t > 10$. Therefore, the chimera states evolved at $t > 10$ as the oscillators were roughly divided into a coherent area and an incoherent area according to values of $l_j(t)$. In the final example, the incoherent area dominated since the values of the local parameters were lower than 0.5.

The time trace of local order parameters provides a useful indicator for qualitatively evaluating the chimera states. However, it is not a straightforward task to determine the side length $2\delta + 1$ of the local region surrounding each oscillator. The larger the value of δ , the more global coherent domains will be captured; however, incoherent domains will also merge into the global coherent domains. Meanwhile, with a smaller δ value, while more incoherent and spatial domains will be identified, the global coherent domains will not be recognized. We thus decided that the key aspect of characterizing the chimera states is to examine the coexistence of two different domains separated in space, where one part of the oscillator network is operating coherently while the other exhibits incoherent behavior. This encouraged us to employ the topological method to characterize the coherent and incoherent domains. By using the time-variant topological features to track the time trace of these domains, we could better understand how chimera states are evolved, which would allow for a qualitative prediction of the chimera states in the early stage of the dynamics.

Here, we present a mapping to transform the j th oscillator to a point cloud on a torus surface

$$\varphi : \theta_j \rightarrow (x_{\theta_j}, y_{\theta_j}, z_{\theta_j}), \quad (7)$$

where

$$x_{\theta_j} = (R_m + R_p \cos \theta_j) \cos\left(\frac{2\pi j}{N}\right), \quad (8)$$

$$y_{\theta_j} = (R_m + R_p \cos \theta_j) \sin\left(\frac{2\pi j}{N}\right), \quad (9)$$

$$z_{\theta_j} = R_p \sin \theta_j. \quad (10)$$

In our simulations, we set the major radius R_m and minor radius R_p of the torus as $R_m = 4$ and $R_p = 1$, respectively. This mapping demonstrated that we can use higher-order topological structures such as loops to evaluate the chimera states of oscillator systems. For example, in the global synchronized state, the mapped points will tend to be distributed along one major loop on the torus surface, while more minor loops will be formed with the increase in incoherent regions.

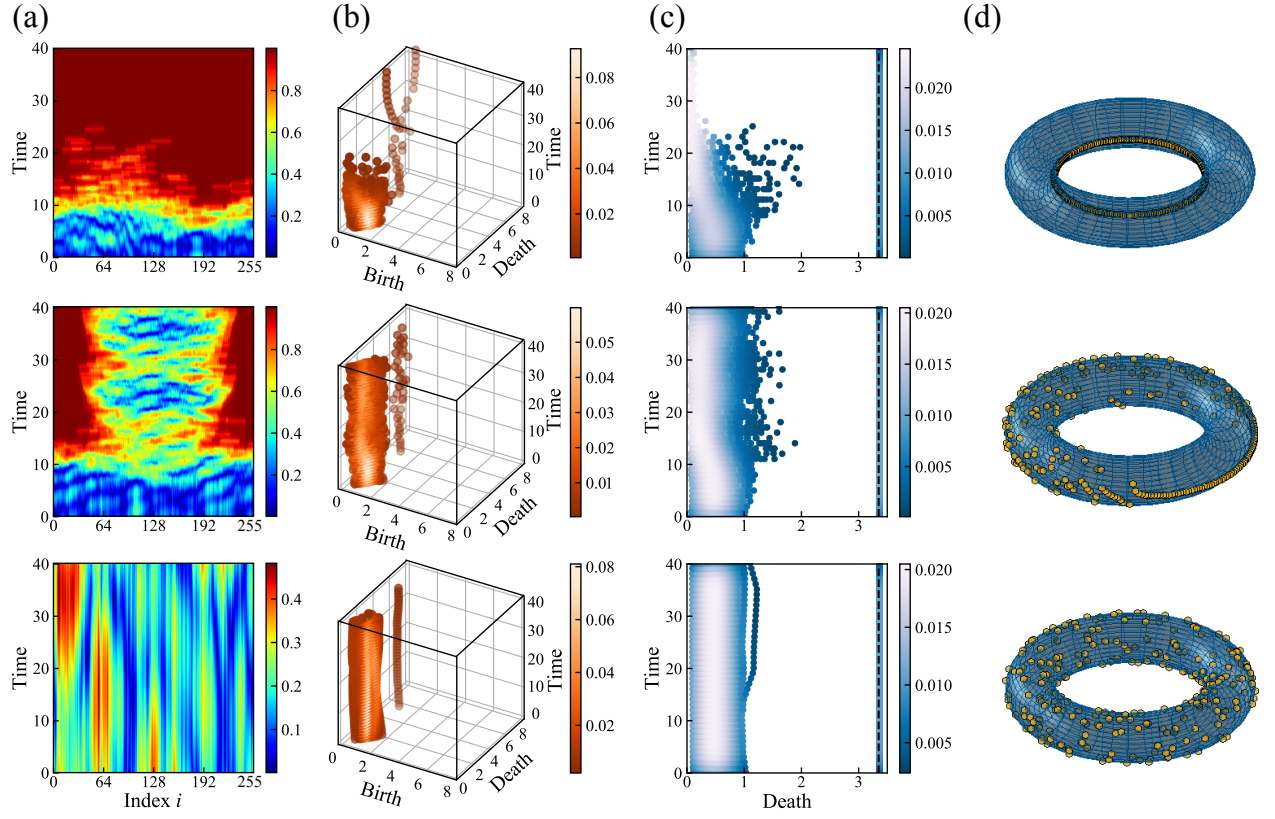


FIG. 5. Three examples of different phase dynamics: synchronized state (top row), chimera state (middle row), and asynchronous state (bottom row) along the evolution timeline. Their differences can be evaluated by (a) the time trace of local order parameters, or time-variant topological features such as (b) the three-dimensional persistence diagrams of loop patterns, and (c) the distribution of the death radii of the connected components appearing along the evolution timeline. Persistence diagrams were obtained from the mapped points of the oscillator phases on a torus surface. (d) The shape of the mapped points corresponds with each phase of dynamics at $t = 40$.

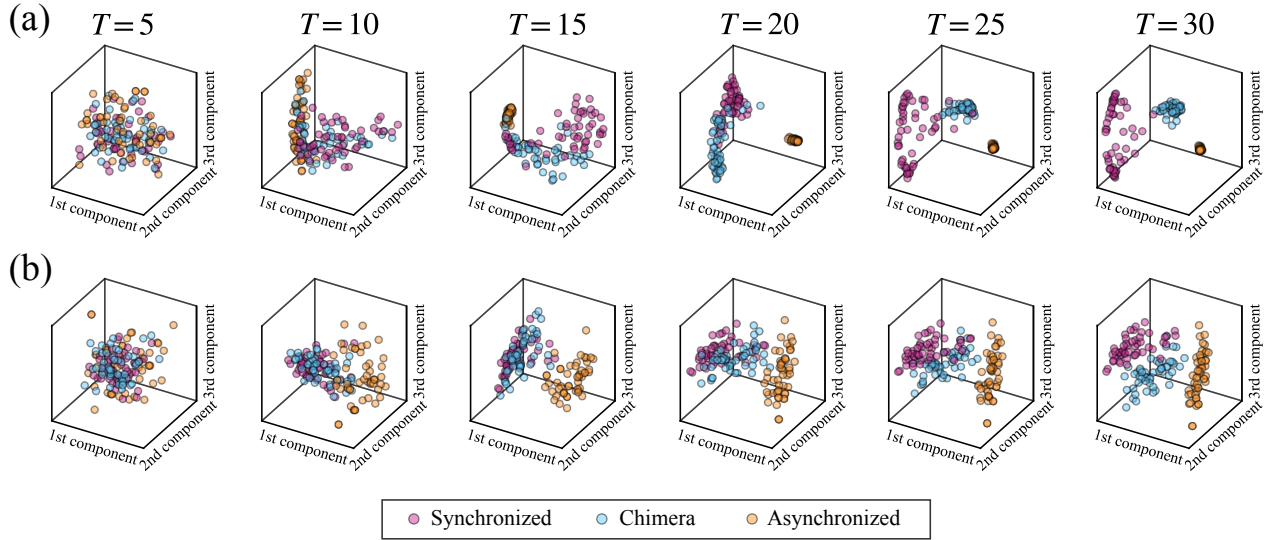


FIG. 6. The dimensional reduction of topological similarity features for (a) connected components (top row), and (b) loops (bottom row) via kernel principal component analysis. These figures represent the distribution of each dynamical case when $T = 5, 10, 15, 20, 25, 30$ from left to right. Each point represents a synchronized (purple), chimera (blue), and asynchronous state (orange).

Figures 5(b),(c) present the three-dimensional persistence diagrams for the loop patterns and the distribution of the death radii of the connected components appearing along the phase evolution of the oscillators that correspond with the examples in Fig. 5(a). The colored bar for each plot in Figs. 5(b),(c) indicates the density of the points in the corresponding plot. The patterns of the mapped points in three-dimensional space corresponding with these examples at $t = 40$ are illustrated in Fig. 5(d). If the oscillators were in global synchronized states, for example, the top row of Fig. 5(a) at $t \geq 25$, only one loop along the torus tube appeared in the mapped space, meaning we obtained one point in the three-dimensional diagram in Fig. 5(b) for each t . As both coherent and incoherent dynamics emerged in the chimera state in the middle row of Fig. 5, small loops appeared around the minor circles of the torus surface, which means more points were generated along the time axis in the three-dimensional diagram of the loop patterns. As illustrated in the bottom row of Fig. 5, the density of these points in the persistence diagram increased as the incoherent dynamics dominated in the phase dynamics. The differences among the oscillator phase dynamics could also be evaluated by observing the distribution of the death radii of the connected components illustrated in Fig. 5(c). In the global synchronized state, connected components emerged and then quickly merged at almost the same death radii (top of Fig. 5(c)). Conversely, in the asynchronized state, the mapped points of the oscillators on the torus surface were randomly distributed. The death radii were concentrated in the range of 0 to 1, and their distributions were almost the same throughout time-evolving (bottom of Fig. 5(c)). In the chimera state, the death radii of the connected components in the coherent region were smaller than those in the incoherent region, with the death radius exhibiting a wider distribution along the timeline of the chimera state (middle of Fig. 5(b)). It should be noted that time-variant topological features provide a novel means of recognizing chimera states in quantitative terms without having to rely on the tuning parameter δ of the local order parameter.

Next, we demonstrate that the kernel method based on time-variant topological features can also be used to characterize the chimera states in early-stage dynamics. Specifically, we prepared 150 cases of temporal phase data that were differentiated in terms of the initial phase condition. Here, we considered three labels of synchronized, chimera, and asynchronized states, with 50 cases for each state. We relied on the global Kuramoto order parameter $r(t)$ at a sufficiently large t to label the dynamics as synchronized states for $r(t = 40) > 0.85$, chimera states for $0.45 \leq r(t = 40) \leq 0.85$, and asynchronized states for $r(t = 40) < 0.45$. Figure 6 highlights the projection up to the third component of the

kernel principal component analysis for the Gram matrix of a total of 150 three-dimensional persistence diagrams. The purple, blue, and orange points represent the synchronized, chimera, and asynchronized states, respectively. To compute the three-dimensional persistence diagrams, we set the time step as $\tau_1 = 0, \tau_{k+1} - \tau_k = 1$ ($k = 1, 2, \dots, T - 1$). In the initial stages of evolution, such as $T = 5$, it proved difficult to observe any clear differences among the points presenting different behaviors. As T was increased, the separability increased for both kernels using the connected components and loops, even in early stages such as $T = 20, 25$.

IV. CONCLUDING REMARKS AND DISCUSSION

In this paper, we demonstrated that the time-variant topological features constructed from the phase evolution in oscillatory systems can be used to characterize the behavior of the dynamics, even in the early stages of the evolution. Such behaviors include global synchronization, multicluster synchronization, and chimera state emergence, which conventional order parameters fail to sufficiently recognize. This indicates that our topological approach is an effective approach for understanding the phase dynamics of oscillators.

In previous applications of persistent homology in relation to oscillatory systems, only the average temporal patterns were considered [39, 40]. Our approach fundamentally differs from such an approach in that it allows us to trace the temporal patterns, which are more helpful to investigating the specific behavior of dynamics. Furthermore, by combining our approach with the machine learning kernel method, we provided an unsupervised scheme to characterize the phase dynamics without predefined label training. This aspect is highly significant from the physical perspective, since unknown dynamics can be revealed using this unsupervised scheme, including in terms of characterizing the different types of chimera state.

It remains unclear as to whether mapping from a set of oscillator phases to a point cloud can be regarded as optimal mapping. In fact, it can be argued that other mapping methods involving various manifolds could extract more meaningful and higher dimensional topological information. Moreover, in addition to the values of the phases, other information, such as the phase derivatives, could be used to construct the time-variant topological features. In view of this, we expect that our study will be successfully applied to more practical situations in the future, including research involving noisy environments, nonuniform coupling strengths, or asymmetrical network structures, all of which may have oscillator networks with topological configurations that change over time.

-
- [1] T. Chouzeouris, I. Omelchenko, A. Zakharova, J. Hlinka, P. Jiruska, and E. Schöll, *Chaos* **28**, 045112 (2018).
- [2] C. J. Stam, *Nat. Rev. Neurosci.* **15**, 683 (2014).
- [3] A. Fornito, A. Zalesky, and M. Breakspear, *Nat. Rev. Neurosci.* **16**, 159 (2015).
- [4] R. Ferri, S. Miano, O. Bruni, J. Vankova, S. Nevsimalova, S. Vandi, P. Montagna, L. Ferini-Strambi, and G. Plazzi, *Clin. Neurophysiol.* **116**, 2675 (2005).
- [5] C. Dibner, U. Schibler, and U. Albrecht, *Annu. Rev. Physiol.* **72**, 517 (2010).
- [6] B. A. M. Owens, M. T. Stahl, N. J. Corron, J. N. Blakely, and L. Illing, *Chaos* **23**, 033109 (2013).
- [7] N. J. Corron and J. N. Blakely, *Proc. Royal Soc. A* **471**, 20150222 (2015).
- [8] S. H. Strogatz, *Physica D* **143**, 1 (2000).
- [9] H. Edelsbrunner, D. Letscher, and A. Zomorodian, in *Proceedings 41st Annual Symposium on Foundations of Computer Science* (2000) pp. 454–463.
- [10] Q. H. Tran and Y. Hasegawa, *Phys. Rev. E* **99**, 032209 (2019).
- [11] A. Myers, E. Munch, and F. A. Khasawneh, *Phys. Rev. E* **100**, 022314 (2019).
- [12] H. Kim, J. Hahm, H. Lee, E. Kang, H. Kang, and D. S. Lee, *Brain Connect.* **5**, 245 (2015).
- [13] M. Hajji, B. Wang, C. Scheidegger, and P. Rosen, in *2018 IEEE Pacific Visualization Symposium (PacificVis)* (2018) pp. 125–134.
- [14] Q. H. Tran, V. T. Vo, and Y. Hasegawa, *Phys. Rev. E* **100**, 032308 (2019).
- [15] Q. H. Tran, M. Chen, and Y. Hasegawa, *Preprint at arXiv:2004.03169* (2020).
- [16] H. Edelsbrunner and J. Harer, *Computational Topology. An Introduction* (American Mathematical Society, Providence, RI, 2010).
- [17] J. Reininghaus, S. Huber, U. Bauer, and R. Kwitt, in *Proceedings of the 28th IEEE Conference on Computer Vision and Pattern Recognition* (IEEE, Boston, MA, USA, 2015) pp. 4741–4748.
- [18] G. Kusano, Y. Hiraoka, and K. Fukumizu, in *Proceedings of The 33rd International Conference on Machine Learning*, Proceedings of Machine Learning Research, Vol. 48, edited by M. F. Balcan and K. Q. Weinberger (PMLR, New York, New York, USA, 2016) pp. 2004–2013.
- [19] M. Carrière, M. Cuturi, and S. Oudot, in *Proceedings of the 34th International Conference on Machine Learning*, Proceedings of Machine Learning Research, Vol. 70, edited by D. Precup and Y. W. Teh (PMLR, International Convention Centre, Sydney, Australia, 2017) pp. 664–673.
- [20] T. Le and M. Yamada, in *Proceedings of the 32nd International Conference on Neural Information Processing Systems*, NIPS’18 (Curran Associates Inc., USA, 2018) pp. 10028–10039.
- [21] S. Jalan and R. E. Amritkar, *Phys. Rev. Lett.* **90**, 014101 (2003).
- [22] S. Jalan, R. E. Amritkar, and C.-K. Hu, *Phys. Rev. E* **72**, 016211 (2005).
- [23] R. E. Amritkar, S. Jalan, and C.-K. Hu, *Phys. Rev. E* **72**, 016212 (2005).
- [24] A. Arenas, A. Díaz-Guilera, and C. J. Pérez-Vicente, *Phys. Rev. Lett.* **96**, 114102 (2006).
- [25] C. Zhou, L. Zemanová, G. Zamora, C. C. Hilgetag, and J. Kurths, *Phys. Rev. Lett.* **97**, 238103 (2006).
- [26] J. Shawe-Taylor, C. K. I. Williams, N. Cristianini, and J. Kandola, *IEEE Trans. Inf. Theory* **51**, 2510 (2005).
- [27] C. M. Bishop, *Pattern Recognition and Machine Learning* (Springer-Verlag, Berlin, Heidelberg, 2006).
- [28] O. E. Omelchenko, Y. L. Maistrenko, and P. A. Tass, *Phys. Rev. Lett.* **100**, 044105 (2008).
- [29] M. J. Panaggio and D. M. Abrams, *Nonlinearity* **28**, R67 (2015).
- [30] Y. Kuramoto and D. Battogtokh, *Nonlinear Phenom. Complex Syst.* **5**, 380 (2002).
- [31] D. M. Abrams and S. H. Strogatz, *Phys. Rev. Lett.* **93**, 174102 (2004).
- [32] M. R. Tinsley, S. Nkomo, and K. Showalter, *Nat. Phys.* **8**, 662 (2012).
- [33] A. M. Hagerstrom, T. E. Murphy, R. Roy, P. Hövel, I. Omelchenko, and E. Schöll, *Nat. Phys.* **8**, 658 (2012).
- [34] K. Bansal, J. O. Garcia, S. H. Thompson, T. Verstynen, J. M. Vettel, and S. F. Muldoon, *Sci. Adv.* **5** (2019).
- [35] Y. Zhu, Z. Zheng, and J. Yang, *Phys. Rev. E* **89**, 022914 (2014).
- [36] N. Yao, Z.-G. Huang, C. Grebogi, and Y.-C. Lai, *Sci. Rep.* **5**, 12988 (2015).
- [37] M. Wolfrum, O. E. Omelchenko, S. Yanchuk, and Y. L. Maistrenko, *Chaos* **21**, 013112 (2011).
- [38] I. Omelchenko, Y. Maistrenko, P. Hövel, and E. Schöll, *Phys. Rev. Lett.* **106**, 234102 (2011).
- [39] B. J. Stolz, H. A. Harrington, and M. A. Porter, *Chaos* **27**, 047410 (2017).
- [40] S. Maletić, Y. Zhao, and M. Rajković, *Chaos* **26**, 053105 (2016).